ORIGINAL RESEARCH ARTICLE

Modeling Alumina Feeding With the μ(I)-Rheology

SINDRE ENGZELIUS GYLVER and KRISTIAN ETIENNE EINARSRUD

Efficient feeding and dissolution of alumina are necessary in order to maintain a stable Hall–Héroult process. One dose of alumina contains several thousand grains, and simulating the motion of individual particles is in practice impossible. The current work proposes to model the alumina dose through a continuous formulation, using the μ(I)-rheology. The rheology is implemented as a viscosity model in OpenFOAM and initial verification cases showed an average deviation below 0.1 pct, and a benchmark case had an average deviation of 7.4 pct. A parametric study, where grains were simulated to collapse on a flat surface identified the two rheology parameters μ_2 and I_0 to be of particular importance, accounting for more than 70 pct of the variation seen. Finally, three-phase cases simulating the feeding of a dose in cryolite were conducted, and the μ(I)-rheology was able to let the parts of the dose disperse into the melt and detach, which is in accordance with what has been seen in experiments. The current work was also able to couple the model with an earlier developed solidification model, hence, creating a framework for developing a full model for alumina feeding.

https://doi.org/10.1007/s11663-023-02812-6

I. INTRODUCTION

ALUMINUM is produced by the Hall–Héroult process, which is an electrochemical process, conducted in large cells at approximately 960 °C. Alumina powder is dissolved in a bath of molten cryolite and reacts with carbon anodes to produce the metal:

$$2Al_2O_3(diss) + 3C(s) \rightarrow 4Al(l) + 3CO_2(g). \quad [1]$$

In most cells, alumina is added in batches through point feeders, which are located at several positions. As discussed by Lavoie *et al.*,[1] modern cells tend to increase in amperage and hence size, resulting in that one feeder needs to distribute alumina over a larger surface area than earlier . They found that the ratio between amperage and feeder has increased from 50 kA pr feeder to 300 over 30 years. In addition, the anodic–cathodic distance (ACD) is decreasing, resulting in lesser available volume for alumina to dissolve in Ref 1. A batch of alumina might not be dissolved immediately after addition, and so-called rafts might be formed, being a rigid porous body consisting of frozen bath and alumina.[2] A better understanding in how rafts are formed and behave will aid the development of technology for better alumina dissolution and distribution, ultimately resulting in a more efficient process.

Modeling is a valuable tool in aiding our understanding of the alumina addition and several models aim to estimate the alumina distribution in cells , where alumina can be considered to be a concentration,[3–5] Lagrangian particles[6] or a big spherical lump,[7] which can be applied in order to optimize feeder position and addition frequency. Zhan *et al.*[5] consider formation and dissolution of rafts in their model based in Computational Fluid Dynamics (CFD), where an empirical formulation based on experiments is proposed. The model by Bojarevics and Dupuis[6] also accountss for raft formation, but both dimensions and dissolution rates of rafts must be given as input parameters and are, thus, not known.

Models for understanding and predicting how alumina is dissolved are needed in order for the larger model to predict the distribution properly. Studies when assuming alumina to be dispersed spheres indicate that the process can be explained by a shrinking sphere model.[8] Modeling dissolution of a single raft has been done by several authors, by assuming spherical or flat geometries.[9–11]

In practice, however, rafts have been observed to have a more complex geometry in industrial cells,[12] where alumina spreads over the free surface with varying thickness. A similar structure is seen in an analogous model at room temperature,[13] and smaller rafts created in a lab cell[14] were found to have a non-uniform thickness. In addition, the mentioned models are not able to account for how addition method affects the

SINDRE ENGZELIUS GYLVER and KRISTIAN ETIENNE EINARSRUD are with the Department of Material Science and Engineering, NTNU, Alfred Getz' veg 2, 7034, Trondheim, Norway. Contact e-mail: sindre.e.gylver@ntnu.no

Manuscript submitted October 25, 2022; accepted April 26, 2023.
Article published online May 30, 2023.

formation, which is also found to be of importance.[15] In see-through cells,[16] it is observed that rafts form on the top of the surface and smaller parts loosen and snow into the melt.

Recently, Roger *et al.*[17] developed a coupled model in a Lagrangian framework, by using discrete element method (DEM) to determine the movement of the alumina particles, while smoothed particle hydrodynamics (SPH) were used to compute the bath flow. In addition, a heat transfer model based on the heat conduction equation was introduced, and phase change of the bath was modeled using an entalphy method. A drawback with this model is the cost of computational time when the number of particles increases, although it can be improved by parallel computing.

A continuous formulation, however, does not suffer from the same limitations relating to scale up. Furthermore, due to the maturity of the continuous formulations, a large amount of models and sub-models for various physics, for example, turbulence,[18] solidification,[19] mass transfer and Magneto Hydrodynamics,[6] are described in the literature, potentially facilitating further extensions for alumina feeding and dissolution.

The current work aims to study whether the alumina can be expressed with a continuous formulation, where the granular behavior of alumina is expressed by the developed μ(I)-rheology.[20] The model is implemented in the CFD-software OpenFOAM,[21] where it is verified for both single- and multiphase solvers. Further, a parametric study aims to identify the relative importance of the model parameters. Finally, the framework is demonstrated in three-phase alumina-air-bath system, where it also is coupled with a framework allowing for the bath to freeze.

II. THE *M*(I)-RHEOLOGY

Being able to describe granular flow as a continuum is of high benefit for several applications, for example, in predicting avalanches[22] or to model sedimentation[23] and segregation.[24] A problem with these kind of flows is the high variation in flow behavior, ranging from solid like (*i.e.*, not deforming to shear forces) when put at rest, to liquid like when poured or flowing through a pipe.[20] Roughly speaking, granular flows can be separated into dense and dilute (or fluidized) regimes, depending upon the relative distance between particles and the strength of their interactions. The fluidized regime has successfully been described by the kinetic theory for granular flow (KTGF).[25] It is in particular when in the dense regime, with a liquid-like behavior of particles, where there is a lack of good descriptions.

The $\mu(I)$-rheology is a possible approach to explain dense granular flows, which can be derived from relatively simple experiments,[26] and further generalized to a three-dimensional space.[20] With this approach, the granular media can be described as an incompressible fluid, which will then have the following mass and momentum balance:

$$\nabla \cdot \boldsymbol{u} = 0, \tag{2}$$

$$\frac{\partial}{\partial t}\boldsymbol{u} + \nabla \cdot \boldsymbol{u}\boldsymbol{u} = -\frac{1}{\rho}\nabla p + \nabla \cdot \boldsymbol{\tau} + \boldsymbol{g}, \tag{3}$$

$\boldsymbol{u}$ and p are respectively the velocity and pressure, ρ is the density, and $\boldsymbol{g}$ accounts for body forces working on the fluid. The rheology is implemented through the internal stress tensor, $\boldsymbol{\tau}$:

$$\boldsymbol{\tau} = \left(\frac{\mu(I)}{D_2}p\right)\boldsymbol{D}. \tag{4}$$

$\boldsymbol{D}$ is the strain rate tensor

$$\boldsymbol{D} = \left(\nabla \cdot \boldsymbol{u} + \nabla \cdot \boldsymbol{u}^T\right), \tag{5}$$

D_2 is the second invariant of $\boldsymbol{D}$ and $\mu(I)$ is a coefficient of friction, expressed as follows:

$$\mu(I) = \mu_1 + \frac{\mu_2 - \mu_1}{I_0/I + 1}, \tag{6}$$

where μ_1 is a threshold value for when a granular media is approaching a quasi-static state and can be interpreted as angle of repose.[27] μ_2 and I_0 are two other material-dependent properties, cf Jop *et al.*[28] for further discussions on these parameters. I is the inertial number, defined as follows:

$$I = \frac{d\sqrt{2}D_2}{\sqrt{p/\rho}}. \tag{7}$$

Earlier work with this rheology has shown good agreement in cases of collapsing granular columns[29] and avalanches.[22]

The presented model might for some cases be ill-posed for large and small I, and Barker *et al.*[30] have developed a regularized model, which will be applied in this work. Some additional parameters need to be added , as described in Eqs. [8] through [11]. A new expression is defined for a low inertial number:

$$\mu(I) = \begin{cases} \sqrt{\frac{a}{\log\left(\frac{4}{7}\right)}}, & \text{for } I \leq I_1 \\ \frac{\mu_1 I_0 + \mu_2 I + \mu_\infty I^2}{I_0 + I} & \text{for } I > I_1. \end{cases} \tag{8}$$

where a and μ_∞ are new material-dependent constants. I_1 is the lowest number possible where the equations are well posed, and is find by solving the equation:

$$4\left(\frac{I\mu'}{\mu}\right)^2 - 4\left(\frac{I\mu'}{\mu}\right) + \mu^2\left(1 - \frac{I\mu'}{2\mu}\right) = 0, \tag{9}$$

where

$$\mu' = \frac{\mathrm{d}\mu}{\mathrm{d}I}, \quad [10]$$

which can be determined by differentiating Eq. [6]. A is a constant expressed as follows:

$$A = I_1 \left(\frac{a(I_0 + I_1)^2}{(\mu_1 I_0 + \mu_2 I_1 + \mu_\infty I_1^2)} \right). \quad [11]$$

The viscous stress tensor can for an incompressible fluid be expressed as follows:[29]

$$\nabla \cdot \boldsymbol{\tau} = \nabla \cdot [2\rho \nu_{\mathrm{eff}} \boldsymbol{D}], \quad [12]$$

where ν_{eff} is the sum of kinematic and turbulent viscosity. The kinematic viscosity of the fluid is expressed as a generalized Newtonian fluid[31] and can, hence, be implemented to be dependent on other variables, which is beneficial when implementing the μ(I)-rheology.

$$\nu = \left(\frac{\mu(I)}{D_2} \frac{p}{\rho} \right). \quad [13]$$

III. MULTIPHASE FLOW

In this work, the system investigated will consist of several phases, and the Volume of Fluid (VOF) method[32] is applied in order to distinguish them from each other. In this method, a single set of momentum and continuity equations are solved in order to calculate the volume fraction of each phase in each computational cell of the system. For a system with N fluids, the amount of a fluid k is expressed by volumetric fraction, α_k, in each computational cell, which will have the following mass balance:

$$\frac{\partial \alpha_k}{\partial t} + \boldsymbol{u} \cdot \nabla \alpha_k = 0. \quad [14]$$

This equation will be solved for $N-1$ of the fluids, while the last one is solved by the constraint:

$$\sum_{\mathrm{i}}^{N} \alpha_i = 1. \quad [15]$$

The mass and momentum balance can be written as follows:

$$\nabla \cdot \boldsymbol{u} = 0, \quad [16]$$

$$\frac{\partial}{\partial t}(\rho_{\mathrm{m}} \boldsymbol{u}) + \nabla \cdot (\rho_{\mathrm{m}} \boldsymbol{u}\boldsymbol{u}) = -\nabla p + \nabla \cdot \boldsymbol{\tau} + \rho_{\mathrm{m}} \boldsymbol{g}. \quad [17]$$

ρ_{m} is a phase averaged value, defined as follows:

$$\rho_{\mathrm{m}} = \sum_{k}^{N} \alpha_k \rho_k. \quad [18]$$

In this framework, each phase can have its own viscosity model, and thus, being calculated independent of each other before being phase averaged

$$\nu_{\mathrm{m}} = \sum_{k}^{N} \alpha_k \nu_k, \quad [19]$$

and further applied when calculating the shear rate tensor (Eq. [12]).

IV. NUMERICAL REALIZATION

The current framework is implemented in OpenFOAM,[21] where both the single-phase solver pimpleFOAM and the multiphase solvers interFOAM and multiphaseInterFOAM are applied. For all solvers, the pressure–velocity coupling is solved by the PIMPLE algorithm, described in detail by Greenshields and Weller,[33] chapter 5.

The μ(I)-rheology is implemented as an incompressible viscosity model. It is based on source code already available,[34] where the different equations presented in Section II are solved as their own functions, with the following algorithm:

- D_2 and p_{eff} is calculated, where the latter ensures that the pressure is above zero.
- I is calculated as given in Eq. [7].
- If the regularized model is applied, I_1 is solved iterative by Eqs. [9] and [10], followed by solving A, Eq. [11].
- Then, $\mu(I)$ is solved either by Eq. [6] or [8].
- Finally, the kinematic viscosity is calculated by Eq. [13].

V. VERIFICATION OF SOLVERS

A. *Case 1: Inclined Plane*

When considering a single layer case along an inclined plane with an angle θ and boundary conditions as shown in Figure 1, an analytical solution for the velocity profile exists, as derived by Lagrée *et al.*[29]

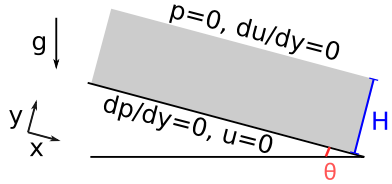

Fig. 1—Sketch of a flow down an inclined plane, where H is the height of the of the column and θ is the incline. Boundary conditions for pressure and velocity are also described in the figure.

$$u = \frac{2}{3} I_\theta \sqrt{g d \cos\theta \frac{H^3}{d^3}} \left[1 - \left(1 - \frac{y}{H} \right)^{3/2} \right]. \quad [20]$$

g is the magnitude of $\boldsymbol{g}$, d is the particle diameter, and H is the height of the column. The inertial number in this case will then be constant:

$$I_\theta = I_0 \left[\frac{\tan(\theta) - \mu_1}{\mu_2 - \tan(\theta)} \right]. \quad [21]$$

The granular media is glass beads, with properties stated in Table I. For these cases, θ is chosen such that I is well posed, and the viscosity model applied in this case, therefore, calculates $\mu(I)$ by Eq. [6]. The cases are set up as 1D cases with cyclic boundary conditions on the in- and outflow, and the rest of the boundary condition on the top and bottom is as described in Figure 1. Four different cases for three different angles θ were ran, described in Table II. In case 1a, the viscosity model is applied with pimpleFoam to verify the model itself. Case 1b is a reproduction of case 1a in interFOAM, where both phases have identical properties, and should in principle yield the single-phase solution, Eq. [20].

Cases 1c and 1d are also two-phase problems, where the effect of overlaying fluids is investigated. In case 1c, the velocity of the granular material should match the analytical solution since the fluid is light. In case 1d, a deviation from the analytical solution is expected to affect the velocity profile for the grains close to the interface.[29]

The mesh had a uniform density of 35 cells/cm in the heights between 0.5 and 4.5 cm, while the density was 60 cells/cm above and below. Numerical schemes are shown in Table III, where cases 1b-d all used the same schemes. In order to reduce the computational time, a velocity field close to the analytical solution (Eq. [20]) was imposed as an initial condition.

Table I. Data Used for Cases 1 and 2 Based on Experiments by Jop *et al.*[28]

Property	Symbol	Value
Particle Diameter	d	0.5 mm
Bulk Density	ρ_s	1500 kg m^{-3}
Rheology Properties	μ_1	0.381
	μ_2	0.643
	I_0	0.279
	μ_∞	0.05
	a	2.1

B. *Case 2: Granular Column Collapse*

A collapse of a granular column into a heap was reproduced from the work of Lagrée *et al.*[29] The system was set up as shown in Figure 2. A quadratic mesh with a uniform size of 0.25 mm was used.

Three cases were run as described in Table IV, where the aspect ratio between height and length, a_0, is defined as follows:

$$a_0 = \frac{L_0}{H_0}, \quad [22]$$

where H_0 and L_0 are the height and half of the length of the column. The two-phase solver interFoam was used, and in this particular case, the viscosity of the mixture was in this case calculated as a harmonic average, same as Lagrée *et al.*[29]:

$$\nu = \frac{1}{\alpha_1/\nu_1 + (1-\alpha_1)/\nu_2}. \quad [23]$$

The density of the surrounding fluid was 1.5 kg m^{-3}, and viscosity was assumed to be constant for each case, stated in Table IV. Gravity is varying between the cases in order to ensure the same conditions as

Table III. The Numerical Schemes Applied in Case 1 and 2

Property	Scheme Single-Phase	Scheme Multiphase
$\frac{\partial}{\partial t}$	backward	forward
$\nabla \boldsymbol{u}$	least squares	least squares
Default Gradient	Gauss linear	Gauss linear
$\nabla \cdot (\boldsymbol{uu})$	linear upwind	linear upwind
$\nabla \cdot (\alpha \boldsymbol{u})$	—	van Leer
Default Divergence	linear	linear
Default Laplacian	Gauss linear	Gauss linear

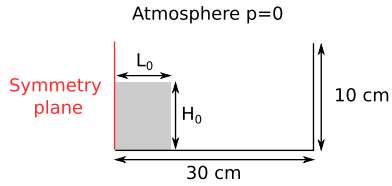

Fig. 2—Setup for the granular column collapse, where the left side is a symmetry plane. Right and lower boundaries are described as a wall, and the top is an atmosphere.

Table II. Summary of the Case 1, Containing Description of the Solver Used, Height of the Granular Material, and Properties of and Height of the Overlapping Fluid, Where Relevant

Property Type	Case 1a Single-phase	Case 1b Multiphase	Case 1c Multiphase	Case 1d Multiphase
ρ_f	—	1500 kg m^{-3}	1 kg m^{-3}	150 kg m^{-3}
ν_f	—	$\mu(I)$	10^{-4} m^2 s^{-1}	10^{-3} m^2 s^{-1}
Granular Column Height	5 cm	2.5 cm	5 cm	5 cm
Fluid Column Height	—	2.5 cm	0.5 cm	0.5 cm

Lagrée *et al.*,[29] which these case are compared with. The same numerical schemes as for the multiphase described in Table III were used.

C. *Results and Discussion*

The results from case 1 are presented in Figure 3, where y is normalized by the column height H, and U is normalized by U_{max}, which is the velocity at $y = H$ in Eq. [20], i.e., the top of the columns. More detailed plots for the upper part of the column for the different angles are provided in Figure 4. The average normalized deviation between the cases and the analytical solutions is presented in Table V.

Table IV. Aspect Ratio, Column Length, L_0 Column Height, H_0, Fluid Viscosity, ν_f, and Gravity, g Used for the Different Cases

Property	Case 2a	Case 2b	Case 2c	Unit
a_0	0.5	1.42	6.26	—
L_0	0.0412	0.03261	0.0155	m
H_0	0.0206	0.0463	0.0972	m
ν_f	0.00120	0.00126	0.00060	$m^2\ s^{-1}$
g	2.06	4.63	9.72	$m\ s^{-2}$

As expected, the velocity profiles for case a–c are in accordance with the analytical solution stated in Eq. [20]. Case 1d deviates from the analytical solution, as the density of the fluid, ρ_f, has increased. This will in turn increase velocity of the grains close to the interface, which is expected.[29] From Figure 4, it seems that the deviation increased at a higher incline, confirmed by the results in Table V. These results verify the model and illustrate that the velocity profile will be affected by fluids, as expected.

The interface between granular material and fluid for selected times are shown in Figure 5.

The overall behavior is similar, although the deviation is smaller at 0.1 and 0.2 s (5.9 and 6.0 pct) than after 0.4 s (10.3 pct). As the numerical frameworks are realized in two different softwares, with differences in schemes and routines, some deviation is expected. The developed

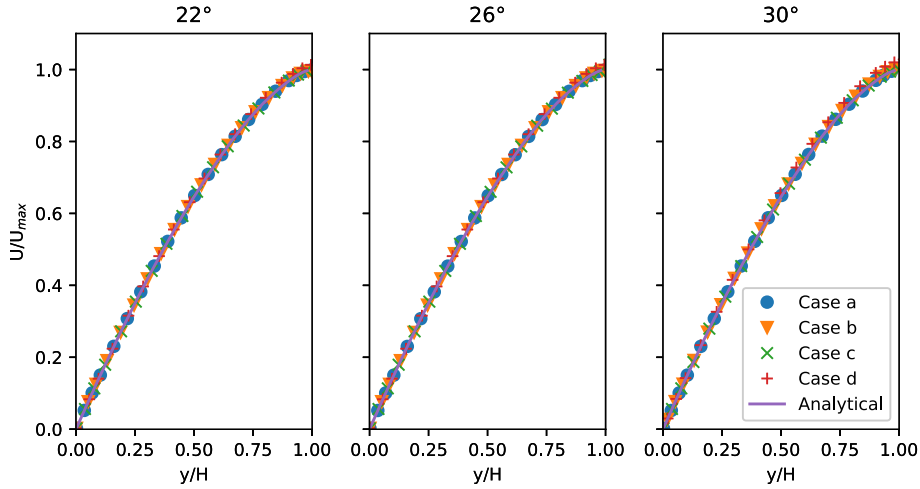

Fig. 3—Velocity profiles of a granular column on an inclined plane for selected angles. Case a: single-phase flow, Case b: multiphase flow with two identical granular phases. Case c: Granular phase with an overlapping fluid with $\rho_f = 1$ kg m^3, Case d: Granular phase with an overlapping fluid with $\rho_f = 150$ kg m^3. The analytical solution U_{max} is calculated by Eq. [20] and H is constant 5 cm for all cases.

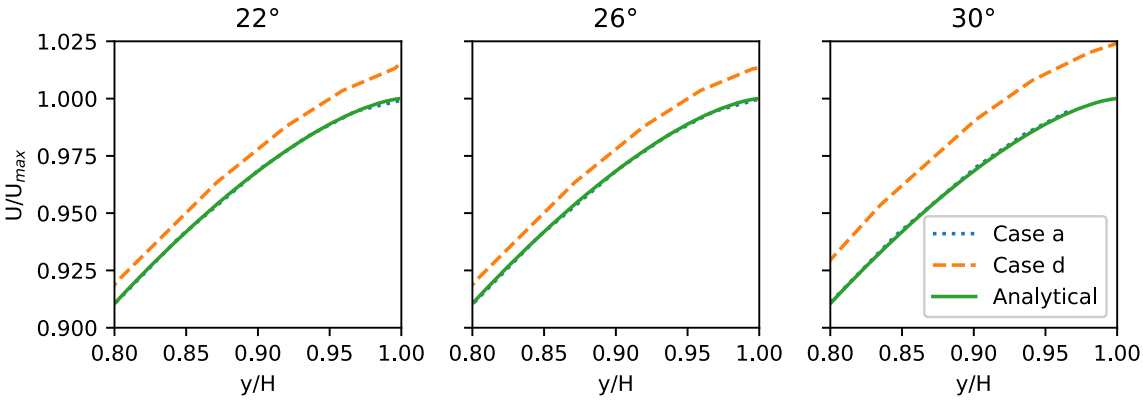

Fig. 4—Detailed view of the velocity profiles shown in Fig. 3 at the highest area of the granular column, containing the analytical solution calculated from Eq. [20]. Case a: single-phase flow case d: Granular phase with an overlapping fluid with $\rho_f = 150$.

Table V. The Average Normalized Deviation Between the Cases and the Analytical Solutions for Case 1

Angle (Deg)	Case 1a (Pct)	Case 1b (Pct)	Case 1c (Pct)	Case 1d (Pct)
22	0.14	0.02	0.02	0.76
26	0.04	0.01	0.04	0.75
30	0.12	0.37	0.13	1.98

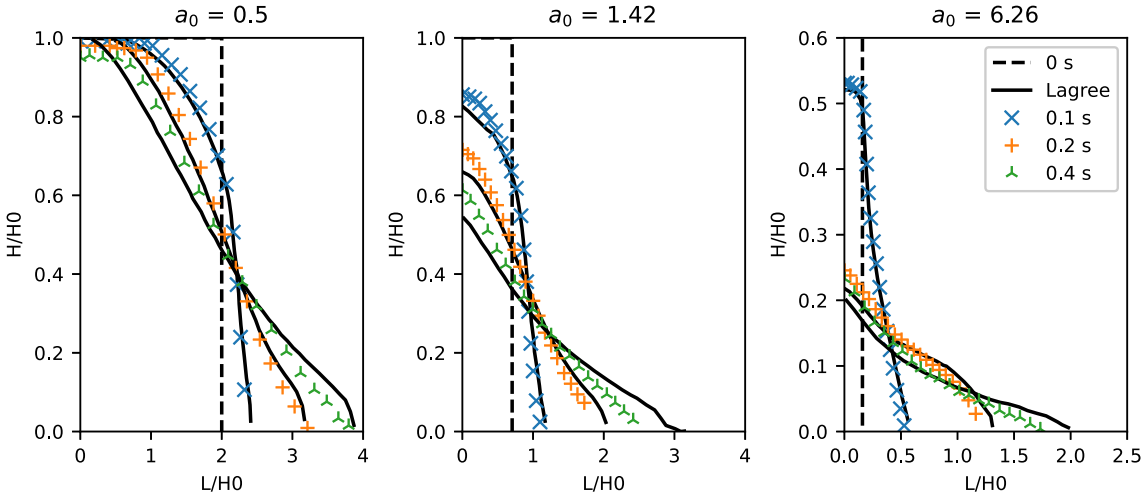

Fig. 5—The grain–air interface during a granular column collapse for selected times, where the aspect ratio given as title.

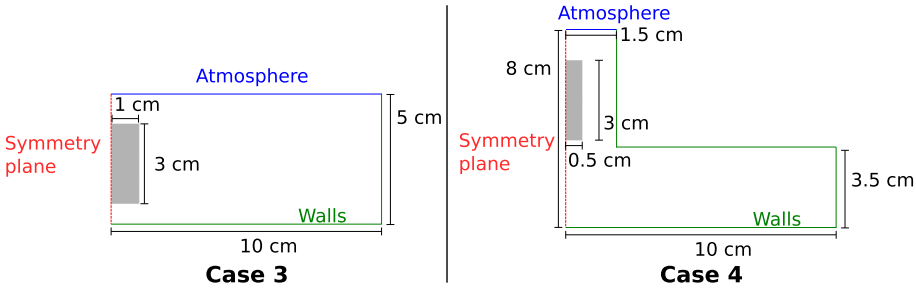

Fig. 6—Setup case 3 and 4, with dimensions and boundary conditions.

Table VI. Boundary Conditions for Cases 3, 4, and 5

Field	Atmosphere	Walls
Velocity	zero gradient	no slip
Pressure	fixed 0	zero gradient
Phase Fraction	zero gradient	zero gradient

model is, therefore, found to be suitable for further investigations.

VI. CASE STUDIES

A. *Cases 3 and 4: Parameter Sensitivity*

A parametric study was conducted in order to quantify its sensitivity and get an overview on what values that might be suitable for alumina. To the authors' knowledge, no experiments for measuring $\mu(I)$-parameters for alumina have been conducted. However, approximately values for bulk density ρ_a,[35] particle diameter d, and angle of repose $\tan^{-1}\mu_1$[36] are known.

The setup is an alumina-air system, shown in Figure 6. All the cases are 2D with evenly spaced quadratic mesh with a length of 0.125 mm. In case 4, the geometry is different as the dose is dropped from a higher distance. However, the mesh has the same resolution as case 3. Boundary conditions are given in Table VI and properties in Table VII.

The studies were set as a 2^k study, where the cases had four factors each. The high and low values are given in Table VIII. The results from case 3 provided the basis for which parameters that will be pursued in case 4, where the fall height and the regularized model are introduced. This is also applied as the value of I_0 is unknown, and hence, allowing for a larger interval of I.

Table VII. Properties for Cases 3, 4, and 5 with References, where Relevant

Property	Symbol	Value case 3	Value case 4	Value case 5	Unit	References
Alumina Density	ρ_a	varies	1200	1200	kg m^{-3}	[35]
Bath Density	ρ_b	—	—	2000	kg m^{-3}	[35]
Gas Density	ρ_g	1	1	1	kg m^{-3}	
Bath Viscosity	ν_b	—	—	10^{-6}	m^2 s^{-1}	[35]
Gas Viscosity	ν_g	$1.48{\cdot}10^{-5}$	$1.48{\cdot}10^{-5}$	$1.48{\cdot}10^{-5}$	m^2 s^{-1}	
Gravity	g	9.81	9.81	9.81	m s^{-2}	
Particle Diameter	d	varies	100	100	μm	[35]
Angle of Repose	$\tan^{-1}\mu_1$	30	30	30	deg	[36]
	$\tan^{-1}\mu_2$	varies	varies	60	deg	
	I_0	varies	varies	1	[-]	
	μ_∞	—	0.05	0.05	[-]	[24]
	a	—	2.1	2.1	[-]	[24]
Drop Height	h	0.5	Varies	0	cm	

Table VIII. The High and Low Values for the Parameters Used in Cases 3 and 4

Property	Low	High	Used in Case
$\tan^{-1}\mu_2$	40 deg	60 deg	3 and 4
I_0	0.1	1	3 and 4
d	20 μm	100 μm	3
ρ	800 kg m^3	1 200 kg m^3	3
h	2 cm	5 cm	4
Model	original	regularized	Case 4

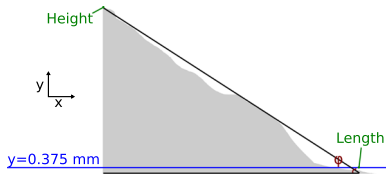

Fig. 7—Sketch illustrating how the length, height, and angle ϕ are defined in cases 3 and 4. The length of the pile is not measured at the bottom, but at $y = 0.375$ mm.

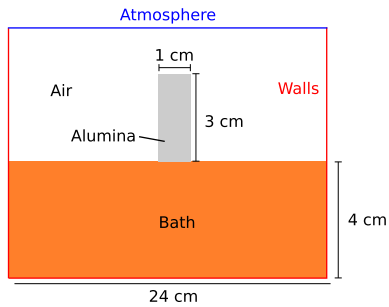

Fig. 8—Setup of case 5, including the initial and boundary conditions.

Statistical analyses were conducted in Minitab, where the responses was set to be the final height of the column and an angle defined by the ratio between height and length of the pile at y = 0.375 mm, sketched in Figure 7. It was chosen not to measure the length of y = 0 as the parts of the phase stretch far out, and the measured angle will not be representative for the shape of the pile.

The goal is to decide which factors, including interactions between them that affect the shape significantly.

B. *Case 5: Three-Phase Case*

The case was simulating parts of the initial stage of alumina feeding, when the dose enters the molten bath, sketched in Figure 8. The mesh is uniform with a cell size of 0.125 mm 4 cm to the left and right, while being graded to become more coarser further out. Time was in this case discretized with a forward Euler scheme, a cubic scheme for the gradients and Fromm's scheme for divergence. One case was run with the μ(I)-rheology, with parameters stated in Table II, chosen based on experience from earlier results.

Two reference cases were run, where the granular media were assumed to be a Newtonian fluid with kinematic viscosity, respectively, 10^{-6} m^2 s^{-1} and 10^{-3} m^2 s^{-1}. The first case is to establish the differences between the developed model and liquid, while the other case with high viscosity is another possible approach to model the solid-state behavior occurring.

The three different cases described in previous paragraph were also conducted in a coarser mesh with cell size of 0.250 mm, in order to investigate grid dependence.

C. *Case 6: Coupled Case*

Case 5 was further extended to account for the possibility for bath to solidify as it gets in contact with the cold dose. This has been investigated in earlier work,[19] and only a brief introduction is, therefore, given.

The energy equation is introduced, written as follows:

$$\frac{\partial}{\partial t}\left(\rho c_{p,m} T\right) + \nabla \cdot \left(\rho_m c_{p,m} \boldsymbol{u} T\right) = \nabla \cdot \left(k_m \nabla T\right) + S_h, \quad [24]$$

where T is the temperature, while $c_{p,m}$ and k_m is respectively the phase average values of heat capacity

Table IX. The Additional Thermal Properties Used for Case 6

Property	Symbol	Value	Unit	References
Alumina Heat Capacity	$c_{p,a}$	1200	J kg^{-1} $°C^{-1}$	[9]
Bath Heat Capacity	$c_{p,b}$	2000	J kg^{-1} $°C^{-1}$	[9]
Gas Heat Capacity	$c_{p,g}$	700	J kg^{-1} $°C^{-1}$	[9]
Alumina Thermal Conductivity	κ_a	8	W $°C^{-1}m^{-1}$	[9]
Bath Thermal Conductivity	κ_b	0.8	W $°C^{-1}m^{-1}$	[9]
Gas Thermal Conductivity	κ_g	0.02	W $°C^{-1}m^{-1}$	[9]
Latent Heat of Fusion	L	530 000	J kg^{-1}	[9]
Temperature constant	T_L	959	°C	N/A
Melting Point	T_M	950	°C	[9]
Damping Strength	C_v	0.1	m^2s^{-1}	N/A
Constant	$\mathcal{A}$	1	—	N/A
Initial Temperature	T_i	960	°C	N/A
Initial Alumina Temperature	T_a	100	°C	N/A

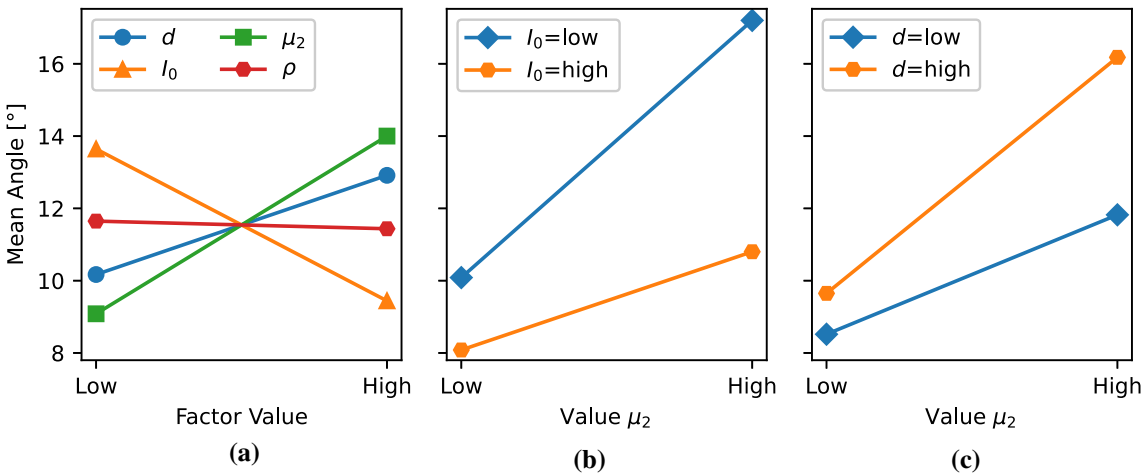

Fig. 9—Plots illustrating how the different parameters affect the final angle of the heap in case 3, measured as illustrated in Fig. 7. *a* the main effects. *b* The interaction plot between μ_2 and l_0. *c*) The interaction plot between μ_2 and d. The values of "high" and "low" are stated in Table VIII.

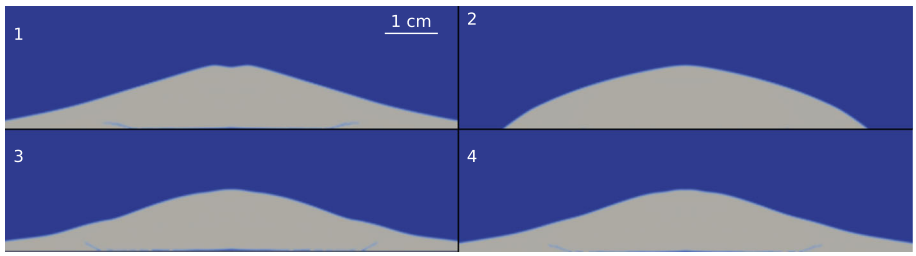

Fig. 10—Heaps of powder after 2 s, an assumed steady state. 1: All factors are high. 2: μ_2 and d high, l_0 and ρ low. 3: μ_2 and d low, l_0 and ρ high. 4: All factors are low.

and thermal conductivity. It is assumed that the phases remain incompressible, and thermal expansion is, hence, neglected.

S_h is a source term that accounts for the change in entalphy due to the phase transition, written as follows:

$$S_h = -\rho L\left[\frac{\partial g_s}{\partial t} + \nabla \cdot (\boldsymbol{u} g_s)\right]. \quad [25]$$

L is the latent heat of fusion, and g_s is the fraction of solidified bath, which is assumed to be isothermal and

expressed as follows:

$$g_s = \begin{cases} \alpha_b & \text{for } T < T_M, \\ 0 & \text{for } T > T_M, \end{cases} \quad [26]$$

where T_M is the melting point and α_b denotes the phase fraction of bath. A modified version of the momentum equation is written as follows:

$$\frac{\partial}{\partial t}(\rho_m \boldsymbol{u}) + \nabla \cdot (\rho_m \boldsymbol{u}\boldsymbol{u}) = \nabla \cdot \boldsymbol{\tau} - \nabla p + \rho_m \boldsymbol{g} + \boldsymbol{S}_d. \quad [27]$$

$\boldsymbol{S}_d$ dampens the relative velocity of the solidifying fluid towards zero and is here implemented as a temperature-dependent viscosity that gains a relatively large value when the fluid becomes solidified:

$$\boldsymbol{S}_d = v_{sol} \cdot \nabla^2 \boldsymbol{u}, \quad [28]$$

where v_{sol} is dependent on temperature,

$$v_{sol} = \begin{cases} \alpha_b C_v & \text{for } T \leq T_M, \\ \alpha_b C_v \exp[\mathcal{A} \cdot (T_M - T)] & \text{for } T_M \leq T \leq T_L, \\ 0 & \text{for } T > T_L. \end{cases} \quad [29]$$

C_v and $\mathcal{A}$ are user-defined constants. In practice, the source term will add an imposed viscosity to the bath phase that increases exponentially from T_L and down to T_M, from zero to C_v, where the exponential formulation is used in order to avoid numerical issues that can arise when the viscosity is rapidly increased.

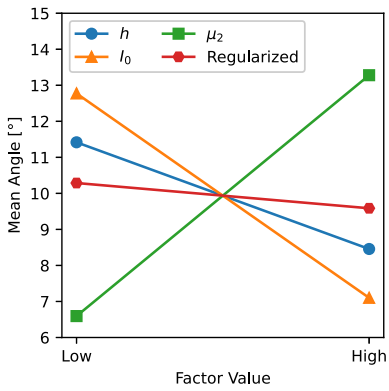

Fig. 11—Plot illustrating how the different factors in case 4 affect the angle of the heap, measured as showed in Figure 7. The values of "high" and "low" are stated in Table VIII.

The same initial conditions (Figure 8) and properties (Table II) as for case 5 are used. The additional thermal properties are presented in Table IX.

VII. RESULTS

A. *Case 3: Initial Parametric Study*

Owing to the dynamic nature of the formulation, the simulated fluids do not reach a complete halt within reasonable simulation times. A quasi-steady state is, however, reached at approximately 2 s, where the shape seems to be stabilized. Changing μ_2 had the largest effect on the angle with a relative contribution of 42.2 pct, followed by I_0 (30.8 pct), d (13.1 pct), as well as the interactions $\mu_2 \cdot I_0$ (8.4 pct) and $\mu_2 \cdot d$ (4.5 pct). Their contributions are visualized in Figure 9, where a) displays the main effects, while b) and c) respectively show the interactions $\mu_2 \cdot I_0$ and $\mu_2 \cdot d$. Figure 10 display the shape of the heap for four selected cases.

B. *Case 4: Extended Parametric Study*

Figure 11 shows a factorial plot for the main effects. The statistical analysis found that μ_2 had the highest relative contribution on the angle with 44.75 pct, followed by I_0 (32.22 pct) $\mu_2 \cdot I_0$ (11.57 pct) and h (8.78 pct). Figure 12 shows a comparison between the original and regularized model, while Table X shows the difference in angles between them for all cases.

Table X. The Measured Angles and Their Difference for the Original and Regularized μ(I)-Model. + Represents that the Factor is Set to a High Value, while - is for a Low Value

h	I_0	μ_2	Original	Regularized	Difference
+	+	+	7.54	6.85	0.68
+	+	–	4.87	4.52	0.36
+	–	+	16.66	16.66	0
+	–	–	5.40	5.14	0.27
–	+	+	10.50	10.08	0.43
–	+	–	7.57	4.87	2.70
–	–	+	19.26	18.68	0.58
–	–	–	10.49	9.90	0.59

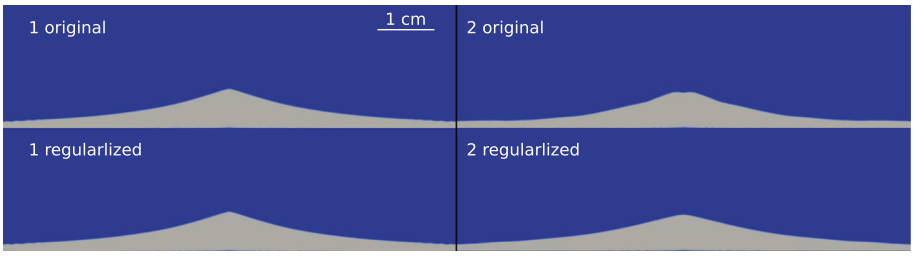

Fig. 12—Heaps of powder after 2 s, an assumed steady state for the original model (upper) and regularized model (below). 1 All other factors are set to their "high" value. 2: μ_2 is "low," h and I_0 are "high" cf. Table VIII for numerical values corresponding to "high" and "low".

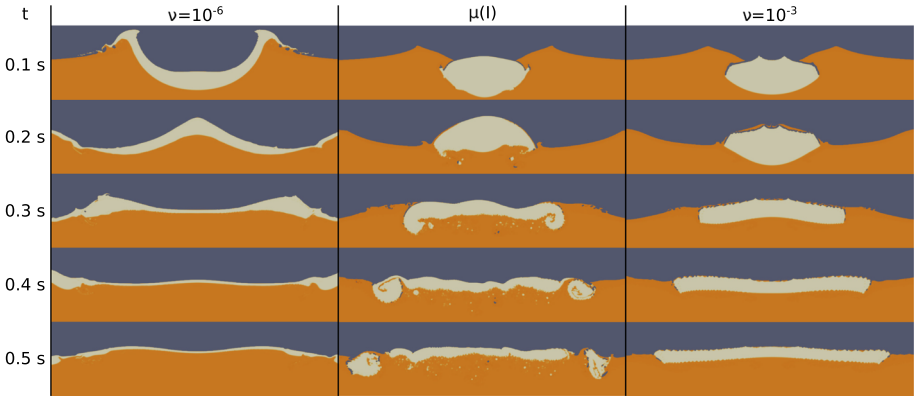

Fig. 13—The phase compositions of blue bath (orange), alumina (beige), air (gray) for selected times, for the following cases: left: Newtonian fluid with $\rho = 1200$ and $\nu = 10^{-6}$. Center: Fluid with the μ(I)-properties given in Table VII. Right: Newtonian fluid with $\rho = 1200$ and $\nu = 10^{-3}$ (Color figure online).

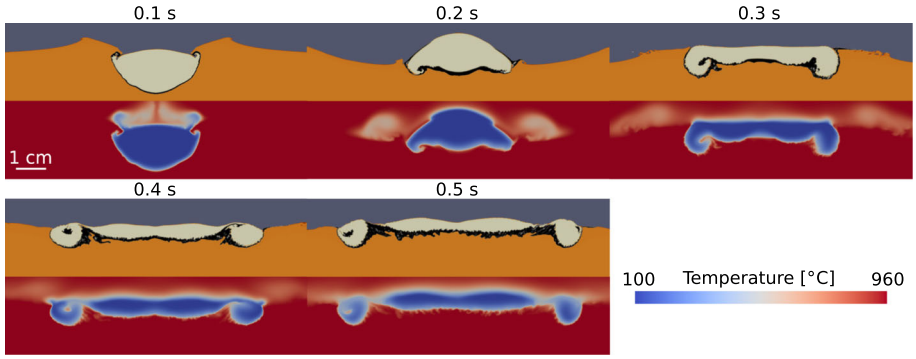

Fig. 14—Phase composition of bath (orange), alumina (beige), air (gray), and frozen bath (black), and temperature field for the coupled case for selected times (Color figure online).

C. *Case 5: Three-Phase Cases*

Snapshots of the μ(I)-rheology is shown in Figure 13, compared with the reference cases. The dose with low viscosity (left) spreads out fast, and parts of the dose flow out of the image. For a high viscous fluid (right), the dose is held together in one piece, which is spread out due to the back wave approaching at t = 0.3. When the μ(I)-rheology is applied (center), small parts are dispersed into the melt, while two big pieces detach from the main dose at t = 0.4.

D. *Case 6: Coupled Case*

Selected images for the coupled case are shown in Figure 14. There is a slight difference in behavior for the case with freezing. Solidification of bath holds the two chunks which were detached together, and it spreads out 8.2 cm in this case, versus 9.1 cm, hence, exhibiting the desired damping effect.

The relative change in thickness and width between the finer and coarser mesh as a function of time is shown in Figure 15

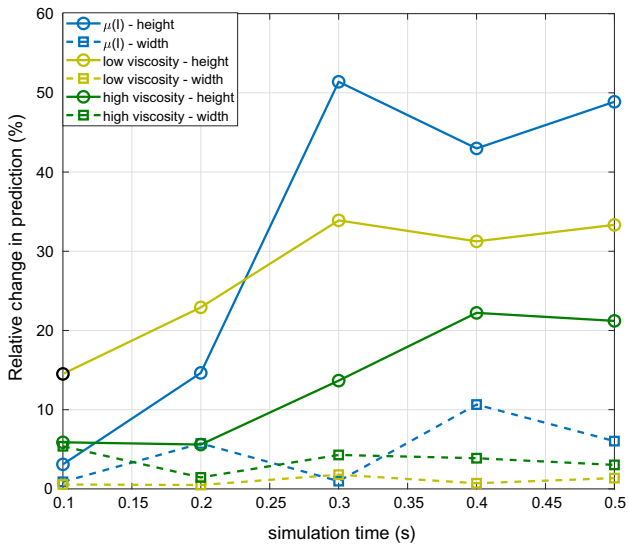

Fig. 15—The relative change in height and width when applying the cases shown in Figure 13 on a coarser mesh.

VIII. DISCUSSION

When μ_2 increases, a higher value of $\mu(I)$ (ref Eq. [6]), and hence, a larger value of v can be obtained. The increased viscosity in the powder will decrease its ability to spread out. The same tendency can be seen from I_0 and d. Increasing I_0 will decrease the value of $\mu(I)$ and v, while an increase of d will increase $\mu(I)$, which can be seen by inserting (7) into (6). μ_2 will increase the possible value $\mu(I)$ while I_0 and d only affect the possible value created, which explain the two interaction effects. ρ was discarded from the model due to low effect. It will have the same effect as d, but since it is affected in lesser magnitude, its effect on $\mu(I)$ will be smaller. The same tendencies for μ_2, I_0 and its interactions are seen in case 4. The increase of spreading with increased drop height is also expected, as higher velocity for the powder when hitting the surface leads to larger spreading of powder.

Applying the regularized model reduced the final angle of the heap, Table X, and the shape will for some cases also be slightly different, as seen on the right images in Figure 12. However, the model did not have a significant impact relative to the other factors in this work. Using the regularized model on case 3 would probably not have changed the results significantly, but it will be applied for the further cases , as it does not affect the computational cost significantly while enabling a broader range of inertial numbers which may occur during the simulations.

The particle size d and density ρ have in these cases quite obvious interpretations for the case of alumina. d will not be uniform and must be interpreted as the average value of a selected dose. The values are, however, not completely independent of each other. For example, reducing the particle size, d, is found to decrease the flowability of alumina and hence increasing the angle of repose,[36] here interpreted as μ_1. The chosen value in this work (30°) represents an alumina with a quite good flowability,[36] and hence, the particle diameter is expected to be high. μ_2 and I_0 do not have such a straightforward interpretation, and estimates of their values for alumina do not exist. This was the reason for large range when setting their "high" and "low" values in cases 3 and 4, ultimately also resulting in high relative effects.

There is limited available experimental data that can be used for comparison of the current cases. Recent images from a master thesis,[37] where alumina was released from a pipe onto a flat plate gave angles at approximately 10°. However, the images are not completely suitable for measuring angles. More experiments should, therefore, be carried out in order to determine parameters. As mentioned above, parameter dependence will probably occur and the particle size should, therefore, be varied in order to get an overview on the range the values might have.

The three-phase cases in Figure 13 illustrate the differences in behavior between the μ(I)-rheology and that of Newtonian fluids with low and high viscosities. While the low viscosity case is included only for comparison, the high viscosity case is introduced as simple alternative which effectively dampens the flow in the granular phase and forms a contained floating raft of comparable size to that obtained with the μ(I)-rheology. However, the high viscosity case produces a more uniform structure, a result of the viscosity being constant. In comparison, the μ(I)-rheology can sustain larger velocity gradients, enabling parts of the granular phase to penetrate into the liquid as seen in the snapshot at 0.3 s flow time. These local "avalanches" of the granular phase between regions of high and low viscosities eventually lead to two fairly large particles breaking off the main raft, as well as smaller grains detaching from earlier similar events. From previous studies of feeding in a water model,[13] a similar tendency with bigger parts of the dose floating away was seen, even when no convection was applied. Furthermore, early dispersion of particles as so-called snowing has also been observed earlier in a see-through cell,[16] indicating that the μ(I)-rheology is indeed able to capture certain features which are not obtained from the high viscosity Newtonian case.

Simulating the dose as a high viscous fluid, showed at the rightmost column in Figure 13, is also presented as a possible approach. It is easier to execute, but it did not allow for parts of the dose to detach, both as smaller flakes and bigger lumps. The resulting raft structure seen at $t = 0.5$ s is uniform for the viscous fluid, while lab experiments[14] suggest that the structure is more irregular, and thus, more similar to the structure achieved by the μ(I)-rheology.

In order to assess the grid dependency of the proposed framework, the simulations shown in Figure 13 were repeated on a mesh with 0.250 mm resolution. The relative change in predicted height and width of the raft is shown in Figure 15 for the selected time steps. Evidently, neither of the simulations are grid converged between these two levels, in particular when considering the raft height, which has a relative change of up to 50 pct for the μ(I)-rheology. However, the relative change is similar for each of the simulations considered, indicating that the μ(I)-rheology does not introduce considerable additional grid dependency.

The results from the coupled case (Figure 14) illustrate that the two developed models can be coupled together. The frozen bath will create a coherent raft and measurements show that in the freezing model slightly dampens the movement. In this case, no smaller parts of powder have detached from the raft, which was the case when only the μ(I)-rheology was applied. In this setup, the initial contact between bath and alumina will cause freezing to occur on the bottom alumina surface, hence, limiting the contact between alumina and the liquid bath. Dropping the dose from an elevation (ref. Case 5), the initial contact surface would be different, resulting in a different final state of the raft.

IX. CONCLUSION AND FURTHER WORK

A framework for simulating the alumina dose through the μ(I)-rheology has been implemented verified and demonstrated in OpenFOAM. The verification is in good agreement with analytical solutions (less than 0.1 pct error on average) and a benchmark case (less than 8 pct error on average).

The parametric studies highlight that the model is quite sensitive with regard to the rheology parameters I_0 and μ_2, which have not been measured for alumina yet. Experiments are needed in order to quantify these parameters further, as well as their dependency on other material parameters.

The two- and three-phase cases illustrate that the μ(I)-rheology exhibits some of the desired features which cannot be realized using a simpler high viscosity Newtonian fluid approach. In particular, the ability to produce a heap-like structure with an actual angle of repose, as well as the complex interaction with fluid surfaces, forming non-uniform rafts and detachment of smaller pieces are qualitatively in good agreement with what is expected from practice.

Coupling the rheology with a model allowing for bath to freeze was successful and shows that frozen bath will form in areas between the alumina pieces, hence, creating a larger coherent raft compared with only applying the μ(I)-rheology. The freezing of bath did also in this case have a limiting effect on the raft shape. Several other sub-models should be implemented in further work, such as infiltration of bath and allowing for the powder to dissolve.

The results presented in the current work demonstrate some of the possibilities for using the μ(I)-rheology to simulate the early interactions between a dose of alumina and molten bath. For future validation studies, further refinements of the mesh should be made in order to more accurately describe the thickness of the raft. Moreover, special attention should be given in order correctly represent interactions between waves on the bath surface and the outer container. As seen for instance in Figure 13, the current system size results in strong reflections from the side walls, influencing the raft shape, which may, or may not, be present in experiments. Further limitations include neglecting surface tension and wetting, and not allowing bath infiltrating in the powder. These issues must be addressed in further work.

While some characteristics relating to alumina feeding are still not implemented, our opinion is that continuum scale models with advanced rheologies could serve as basis for further investigations.

ACKNOWLEDGMENTS

This work has been funded by the SFI Metal Production, (Centre for Research-based Innovation, 237738). The authors gratefully acknowledge the financial support from the Research Council of Norway and the partners of the SFI Metal Production.

FUNDING

Open access funding provided by NTNU Norwegian University of Science and Technology (incl St. Olavs Hospital - Trondheim University Hospital).

CONFLICT OF INTEREST

The authors declare no conflict of interest.

OPEN ACCESS

LIST OF SYMBOLS

d	Particle diameter
ρ_s	Bulk density
μ_1	μ(I)-rheology property
μ_2	μ(I)-rheology property
I_0	μ(I)-rheology property
μ_∞	Regularized μ(I)-rheology property
a	Regularized μ(I)-rheology property
ρ_f	Density of overlapping fluid in case 1
ν_f	Kinematic of overlapping fluid in case 1 and 2
a_0	Aspect ratio in case 2
L_0	Half-length of column in case 2
H_0	Column in case 2
g	Gravity
ρ_b	Bath density
ρ_g	Gas density
ν_b	Bath viscosity
ν_g	Gas viscosity
h	Drop height
$c_{p,a}$	Alumina heat capacity
$c_{p,b}$	Bath heat capacity
$c_{p,g}$	Gas heat capacity
κ_a	Alumina thermal conductivity
κ_b	Bath thermal conductivity
κ_g	Gas thermal conductivity
L	Latent heat of fusion
T_L	Temperature constant
T_M	Melting point
C_v	Damping strength
$\mathcal{A}$	Solidification constant
T_i	Initial temperature in case 6
T_a	Initial alumina temperature

REFERENCES

1. P. Lavoie, M.P. Taylor, and J.B. Metson: *Metall. Mater. Trans. B*, 2016, vol. 47, pp. 2690–96.
2. S.E. Gylver, N.H. Omdahl, S. Rørvik, I. Hansen, A. Nautnes, S.N. Neverdal, K.E. Einarsrud: *Light Metals*, 2019, vol. 2019, pp. 689–96.
3. T. Bardet, S. Foetisch, J. Renaudier, M. Rappaz, Flueck. and M. Picasso: *Light Metals*, 2016, vol. 2016, pp. 315–19.
4. S.T. Johansen, K.E. Einarsrud, A. Solheim, and K.J. Vachaparambil: *Light Metals*, 2022, vol. 2022, pp. 503–11.
5. S. Zhan, M. Jiang, J. Wang, and J. Yang: *Trans. Nonferrous Met. Soc. China*, 2021, vol. 31, pp. 3579–90.
6. V. Bojarevics and M. Dupuis: *Light Metals*, 2022, vol. 2022, pp. 339–48.
7. L. Dion, L.I. Kiss, S. Poncsák, and C.-L. Lagacè: *Metall. Mater. Trans. B*, 2018, vol. 49, pp. 737–55.
8. R.G. Haverkamp and B.J. Welch: *Chem. Eng. Process.*, 1998, vol. 37, pp. 177–87.
9. Kovács, C.J.W. Breward, K.E. Einarsrud, S.A. Halvorsen, E. Nordgård-Hansen, E. Manger, A. Münch, and J.M. Oliver: *Int. J. Heat Mass Transfer*, 2020, vol. 162, p. 120232.
10. V. Dassylva-Raymond, L.I. Kiss, S. Poncsak, P. Chartrand, J.-F. Bilodeau, and S. Guérard: *Light Metals*, 2014, vol. 2014, pp. 603–08.
11. R. Hovland, S. Rolseth, and A. Solheim: *Proc. Intl. Symp. Light Metals Process. Appl.*, pp 3–16.
12. S.E. Gylver, N.H. Omdahl, A.K. Prytz, A.J. Meyer, L.P. Lossius, and K.E. Einarsrud, *Light Metals*, 2019, vol. 2019, pp. 659–66.
13. Gylver, S. Aase, S. Bekkevoll, S.A.K. Forberg, and K.E. Einarsrud: *Light Metals*, 2022, pp. 357–62.
14. S.E. Gylver, A. Solheim, H. Gudbrandsen, Å.H. Follo, and K.E. Einarsrud: *Light Metals*, 2020, vol. 2020, pp. 659–63.
15. A.N. Bagshaw, and B.J. Welch: *Essential Readi. Light Metals*, 2016, vol. 1, pp. 783–87.
16. L. Bracamonte: PhD, Norwegian University of Science and Technology, 2022.
17. T. Roger, L. Kiss, L. Dion, S. Guérard, J.F. Bilodeau, G. Bonneau, R. Santerre, and K. Fraser: *Light Metals*, 2022, vol. 2022, pp. 363–70.
18. K.E. Einarsrud, I. Eick, W. Bai, Y. Feng, J. Hua, and P.J. Witt: Appl. Math. Model., 2017, vol. 44, pp. 3–24.
19. S.E. Gylver and K.E. Einarsrud: *Light Metals*, 2023 (in press).
20. P. Jop, Y. Forterre, and O. Pouliquen: *Nature*, 2006, vol. 441, pp. 727–30.
21. OpenCFD: OpenFOAM ®- Official home of The Open Source Computational Fluid Dynamics (CFD) Toolbox. http://www.openfoam.com. Accessed 6 May 2019.
22. E.P. Montellà, J. Chauchat, B. Chareyre, C. Bonamy, and T.J. Hsu: *J. Fluid Mech.*, 2021, vol. 925, p. A13.
23. J. Chauchat, Z. Cheng, T. Nagel, C. Bonamy, and T.-J. Hsu: *Geosci. Model Dev.*, 2017, vol. 10, pp. 4367–92.
24. T. Barker, M. Rauter, E.S.F. Maguire, C.G. Johnson, and J.M.N.T. Gray: *J. Fluid Mech.*, 2021, vol. 909, p. A22.
25. D. Gidaspow: *Multiphase Flow and Fluidization: Continuum and Kinetic Theory Descriptions*, Academic Press, San Diego, 1994.
26. G.D.R. MiDi: *Eur. Phys. J. E*, 2004, vol. 14, pp. 341–65.
27. M. Tankeo, P. Richard, and É. Canot: *Granular Matter*, 2013, vol. 15, pp. 881–91.
28. P. Jop, Y. Forterre, and O. Pouliquen: *J. Fluid Mech.*, 2005, vol. 541, p. 167 (2005).
29. P.-Y. Lagrée, L. Staron, and S. Popinet: J. Fluid Mech., 2011, vol. 686, pp. 378–408.
30. T. Barker and J.M.N.T. Gray: *J. Fluid Mech.*, 2017, vol. 828, pp. 5–32.
31. R.B. Bird: *Transport Phenomena*, 2nd edn., Wiley, New York, 2002.
32. C.W. Hirt and B.D. Nichols: *J. Comput. Phys.*, 1981, vol. 39, pp. 201–25.
33. C. Greenshields, H. Weller: Notes on Computational Fluid Dynamics: General Principles, https://doc.cfd.direct/notes/cfd-general-principles/, Accessed 19 Sept 2022.
34. A. Jarosch: Incompressible μ(I) rheology for OpenFOAM, https://github.com/alexjarosch/OpenFOAM-muI. Accessed 19 Sept 2022.
35. K. Grjotheim, H. Kvande, eds.: *Introduction to Aluminium Electrolysis*, Aluminium-Verlag, Düsseldorf, pp. 61–86, 1993.
36. B.E. Raahauge, F.S. Williams: *Smelter Grade Alumina from Bauxite: History, Best Practices, and Future Challenges*, Springer, Cham, 2022, pp. 577–648.
37. S. Bekkevoll: MSc, Norwegian University of Science and Technology, 2022.